Materials Advances

ROYAL SOCIETY OF CHEMISTRY

PAPER

View Article Online
View Journal | View Issue

Cite this: *Mater. Adv.*, 2025, 6, 8529

Performance improvement of a thin film thermoelectric generator *via* optimisation of the deposition parameters

Nurfarhana Ahmad Musri,*[a] Yoganash Putthisigamany,[a] Puvaneswaran Chelvanathan,[a] Nadhrah Md Yatim,[b] Farah Liana Mohd Redzuan[c] and Ubaidah Syafiq *[a]

Received 29th July 2025,
Accepted 5th October 2025

DOI: 10.1039/d5ma00823a

rsc.li/materials-advances

Thin film thermoelectric generators (TEGs) offer a compact and scalable solution for harvesting waste heat in microelectronic and flexible systems. However, their performance is highly influenced by material properties, fabrication parameters, and device geometry. This work presents a systematic optimization of Bi_2Te_3 and Sb_2Te_3 thin films for a high-performance TEG. The thin films were deposited *via* radio frequency (RF) magnetron sputtering under varying power conditions and characterized using XRD, FESEM, EDX, Hall measurements, and Seebeck coefficient analysis. The optimal sputtering powers were identified as 75 W for Bi_2Te_3 and 30 W for Sb_2Te_3, yielding high crystallinity and balanced electrical conductivity with favourable Seebeck values. A thin film TEG consisting of six n-type/p-type leg pairs was fabricated using these conditions and subjected to post-deposition annealing to improve performance. The TEG annealed at 200 °C demonstrated a peak power output of 0.84 μW at ~120 °C ΔT, indicating enhanced crystallinity and reduced internal resistance. Dimensional optimization further revealed that wider and shorter TE legs significantly improve the output by minimizing internal resistance. The results highlight the importance of integrating material, process, and device-level optimization for the development of efficient and scalable thin film thermoelectric systems.

1. Introduction

The universal quest for sustainable and efficient energy technologies has intensified interest in thermoelectric generators (TEGs), which offer a direct, solid-state method for converting thermal energy into electricity.[1–6] Among various energy conversion technologies, thermoelectrics stand out due to their reliability, lack of moving parts, and ability to harvest low-grade waste heat,[7,8] making them highly attractive for applications ranging from industrial energy recovery to autonomous sensors and wearable devices.

Bismuth telluride (Bi_2Te_3) and antimony telluride (Sb_2Te_3) are among the most extensively studied thermoelectric materials for near-room-temperature applications, owing to their high Seebeck coefficients, moderate electrical conductivity, and inherently low thermal conductivity.[9,10] The efficiency of a thermoelectric material is governed by its figure of merit (ZT), which is strongly influenced by electrical conductivity (σ), Seebeck coefficient (S), and thermal conductivity (κ), defined as $ZT = (S^2\sigma T)/\kappa$, where $S^2\sigma$ can be defined as power factor (PF). Numerous studies have focused on enhancing the thermoelectric performance to widen its potential and application. Recent efforts have shifted toward thin-film configurations, where these properties can be finely tuned through nanoscale control, improved carrier mobility, and phonon scattering mechanisms. Compared to bulk counterparts, thin-film TEGs offer several advantages, including enhanced power density, mechanical flexibility, and better integration with microelectronic and wearable systems.[11,12]

However, achieving optimal performance in thin-film TEGs requires a multifaceted approach. Key factors such as sputtering parameters, post-deposition treatments, and geometric design must be precisely engineered to maximize electrical output while minimizing internal resistance and thermal losses. Recent advances in Bi_2Te_3 and Sb_2Te_3 thin films have demonstrated that careful control of film microstructure, stoichiometry and strain can markedly improve thermoelectric performance. For example, Zheng *et al.*[13] demonstrated a textured, flexible Bi_2Te_3 thin-film design that achieved record room-temperature ZT values (~1.2) while retaining mechanical

[a] *Solar Energy Research Institute (SERI), Universiti Kebangsaan Malaysia, Bangi, Selangor, Malaysia. E-mail: ubaidahsyafiq@ukm.edu.my*
[b] *Faculty of Science and Technology, Universiti Sains Islam Malaysia, Bandar Baru Nilai, Negeri Sembilan, Malaysia*
[c] *Malaysia-Japan International Institute of Technology, Universiti Teknologi Malaysia, Kuala Lumpur, Malaysia*

robustness, underscoring the importance of crystallographic texture and film processing. In Sb_2Te_3-based systems, strategies such as lattice-strain engineering and heterostructuring have been shown to enhance the Seebeck coefficient and power factor by modifying carrier scattering and phonon transport.[14] Other than that, Haidar *et al.*[15] investigated the effects of sputtering temperature, co-sputtering techniques, and annealing treatments on the structural and thermoelectric properties of these materials for micro-scale TEGs. While their work provides valuable insights into the material-level optimization for vertical μTEG architectures, it does not address planar thin-film device configurations. Nevertheless, collectively, these material-level developments motivate our integrated experimental study to optimize Bi_2Te_3/Sb_2Te_3 thin film TEG performance.

Prior studies have shown that device geometry can strongly influence output power and power density. Kalil *et al.*[16] conducted a detailed performance comparison of bulk TEGs by analyzing different leg geometries under constant leg volume, demonstrating that variations in leg shape and aspect ratio significantly affect power output and thermal management. However, their study focuses exclusively on bulk TEGs, where heat flow and mechanical constraints differ considerably from those in thin-film systems. Several studies combine numerical optimization with experiments to identify optimal leg geometries for thin film or wearable TEGs. For instance, Kuang *et al.*[17] investigated annular thin film TEG architectures and highlighted the combined role of material properties and geometry on device performance, reporting that annealing improves the film Seebeck coefficient and conductivity, while geometry sets the achievable output power density. Mathematical and numerical studies by Newbrook *et al.*[18] further showed that fill factor and interconnect conductivity critically determine thin film TEG performance. Building on this line of work, this study extends the understanding of thin film TEG design by focusing on planar devices, fabricated using optimized sputtering and annealing conditions, and introduces dimensional optimization of the thermoelectric legs.

In this work, we present a comprehensive investigation on the optimization of the deposition parameters for the fabrication of Bi_2Te_3/Sb_2Te_3 thin film TEGs. This study explores the influence of sputtering power on film crystallinity and thermoelectric properties, the impact of post-deposition annealing on device performance, and the role of leg geometry in enhancing power output. By systematically examining each of these factors, this research aims to establish a set of process guidelines for the fabrication of high-performance thin film thermoelectric devices, contributing towards the development of a scalable and cost-effective energy harvesting solution.

2. Materials and methods

2.1. Deposition of thermoelectric films

Bi_2Te_3 and Sb_2Te_3 thin films were deposited using RF magnetron sputtering on soda lime glass (SLG) substrates that were ultrasonically cleaned with methanol, acetone, ethanol, and deionized water for 10 min. Nitrogen gas, a hot plate, and a UV ozone cleaner were also used to eliminate residues from the substrates. A sputter target of Bi_2Te_3 (diameter 50.8 mm, thickness 4.25 mm, 99.999% purity) and Sb_2Te_3 (diameter 50.8 mm, thickness 6.35 mm, 99.999% purity), with argon gas (99.99% purity), were used for the sputter coating. The samples were deposited without substrate heating using RF powers of 75, 90, 105, 120, and 135 W (labelled as A1, B1, C1, D1, and E1) for Bi_2Te_3 at a deposition time of 60 min, and 10, 20, 30, 40, and 50 W (labelled as A2, B2, C2, D2, and E2) for Sb_2Te_3 at 120 min. A longer deposition time was required for Sb_2Te_3 due to the lower RF power limit imposed by the sputtering system. Due to the semiconducting nature and low thermal conductivity of Sb_2Te_3, operating at high RF power sputtering leads to localized heating at the target surface.[19] In our system, insufficient cooling at the sputter gun further worsened this issue, resulting in thermal instability and risk of target degradation. Therefore, a lower power range was used with an extended deposition time to achieve a film thickness comparable to that of the Bi_2Te_3 layer. Although film thickness is a critical factor influencing thermoelectric performance, particularly in thin film configurations, a detailed investigation of its effect lies beyond the current scope of this study. The details of the deposition protocol are extensively discussed in our previous work.[20]

X-ray diffraction (XRD, X'pert-pro PANalytical X-ray diffractometer) using Cu Kα radiation (λ = 1.5406 Å) was used to investigate the phase structure of all the as-deposited thin films. Rietveld refinement of the experimental XRD data was done to calculate lattice parameters *a* and *c*. The field-emission scanning electron microscopy (FESEM/JEOL, JSM7800F, operating at 3.0 kV) topographic and cross-sectional images were used to evaluate the surface microstructure and film thickness. Energy dispersive X-ray spectroscopy (EDX) attached to the FESEM was used to confirm the film composition. Moreover, the Hall effect measurement system (HMS ECOPIA 3000) with a fixed magnetic field of 0.57 T was employed to test the carrier concentration and electrical conductivity. The temperature-dependent in-plane *S* was measured using a Linseis LSR-3, with rectangular samples (about 2 cm × 1.25 cm) mounted for measurement. The absolute *S* was determined in a two-contact configuration relative to a Pt standard, applying a temperature gradient of approximately 25 °C.

2.2. Fabrication of the Bi_2Te_3/Sb_2Te_3 thin film TEG

The TEG consists of 6 pairs of n-type Bi_2Te_3 and p-type Sb_2Te_3 materials, fabricated under the optimal conditions based on the above experiments, with Bi_2Te_3 deposited at 75 W for 60 min, while Sb_2Te_3 at 30 W for 120 min. The TE legs were deposited on a rectangular SLG substrate of 1 mm thickness. A Kapton mask was applied to define specific deposition areas and then n-type Bi_2Te_3 was deposited *via* sputtering. A second Kapton mask was applied to enable the subsequent deposition of p-type Sb_2Te_3 legs in the alternating region. Finally, metallic silver (Ag) contacts were deposited to electrically connect the TE legs, completing the TEG structure (refer Fig. 2(a)). The mask-assisted sequential deposition ensures precise patterning and

alignment of thermoelectric elements and contacts. The complete process flow of TEG fabrication is described in detail in our previous work.[21]

2.2.1. Post-deposition annealing of the of Bi_2Te_3/Sb_2Te_3 thin film TEG. A TEG consisting of legs with a standard design based on Isotta *et al.*[8] (2022) (width of 3 mm and length of 15 mm on a 7.6 cm × 2.5 cm substrate) was used to study the effect of post-deposition annealing on the performance of the TEG. The same TEG sample was annealed sequentially at 100 °C followed by 200 °C, allowing for the evaluation of progressive thermal effects on the same device. A tube furnace was used to anneal the TEG, purged with nitrogen to establish an inert atmosphere, and the sample was then annealed under vacuum conditions. The furnace temperature was increased gradually at a rate of 10 °C per minute until the desired annealing temperature was reached. Each temperature set was maintained for 60 minutes to allow for controlled thermal processing.

2.2.2. Dimensional optimization of the of Bi_2Te_3/Sb_2Te_3 thin film TEG. To investigate the effect of geometry on device performance, several dimensional variations of the thin film TEG were designed using only Sb_2Te_3 as the thermoelectric material. Four alternative patterns were fabricated with respect to the standard design: pattern I reduced the leg width to 1.5 mm; pattern II increased the width to 4.5 mm: pattern III extended the leg length to 25 mm; and pattern IV further increased the length to 35 mm (refer to Fig. 1). These variations were designed to evaluate how changes in leg width and length affect thermal and electrical resistance, and ultimately, power output. This dimensional study enables the identification of optimal TEG leg geometry for improved device efficiency.

2.3. Performance analysis of the thin film TEG

Open-circuit voltage (V_{oc}) as a function of temperature difference (ΔT) and current–voltage–power (IVP) characteristics were recorded using a custom setup shown in Fig. 2(c). A hot plate was used as the heat source, and a metal plate was used as the heat sink (without active cooling). All performance measurements were conducted under ambient conditions; the voltage generated by the devices was measured using a Keithley Agilent 34401A voltmeter, and temperature differences were monitored using a Fluke Ti32 thermal camera. The T_h and T_c values were taken near the TE legs as shown in Fig. 2(b). For the IVP measurement, a FLUKE 8846A (ammeter) and a variable resistor were added. All measurements were performed under a fixed temperature gradient, with the hot side maintained at approximately 150 °C and the cold side left to cool passively. The power curve of the TEG was derived and plotted using $P = VI$ after I–V values were recorded across a range of resistances.

3. Results and discussion

3.1. Characterization of Bi_2Te_3 and Sb_2Te_3 thin films

The phase purity and crystallinity of the thin films were measured using the X-ray diffraction (XRD) technique. The ''substrate'' curve represents the diffraction pattern of the bare substrate, confirming that other peaks observed in the spectra

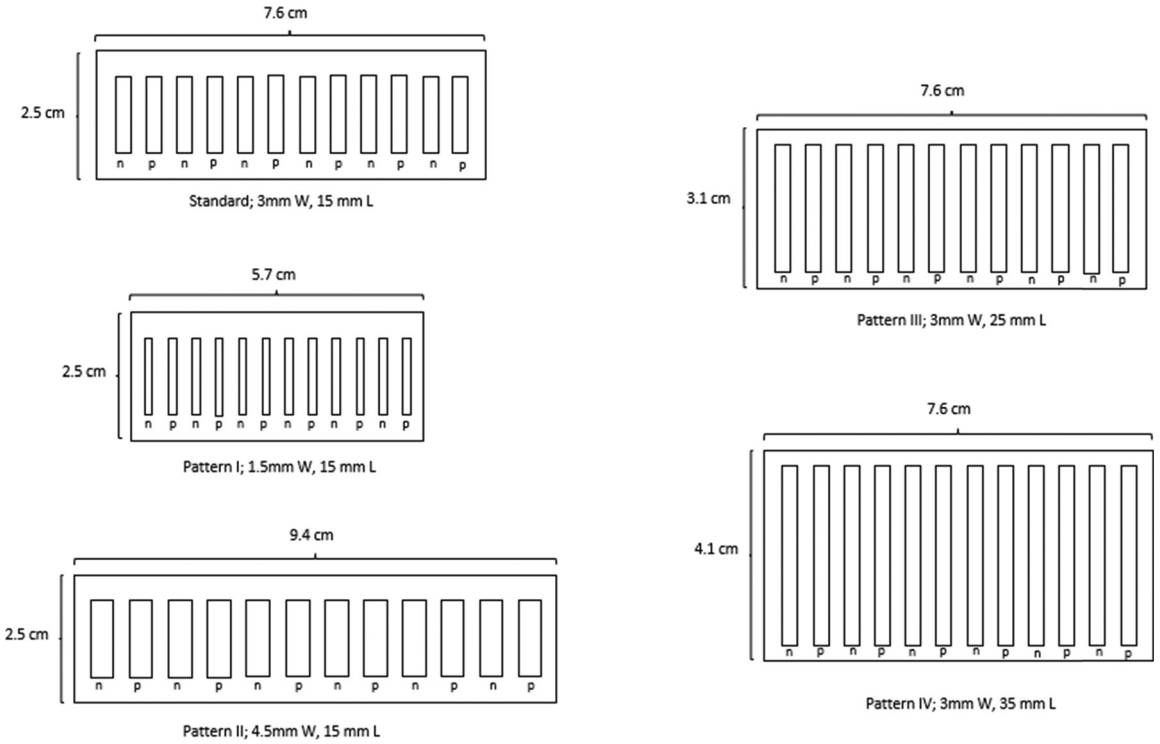

Fig. 1 Illustration of the dimension variation tested for the Sb_2Te_3-only thin film TEG.

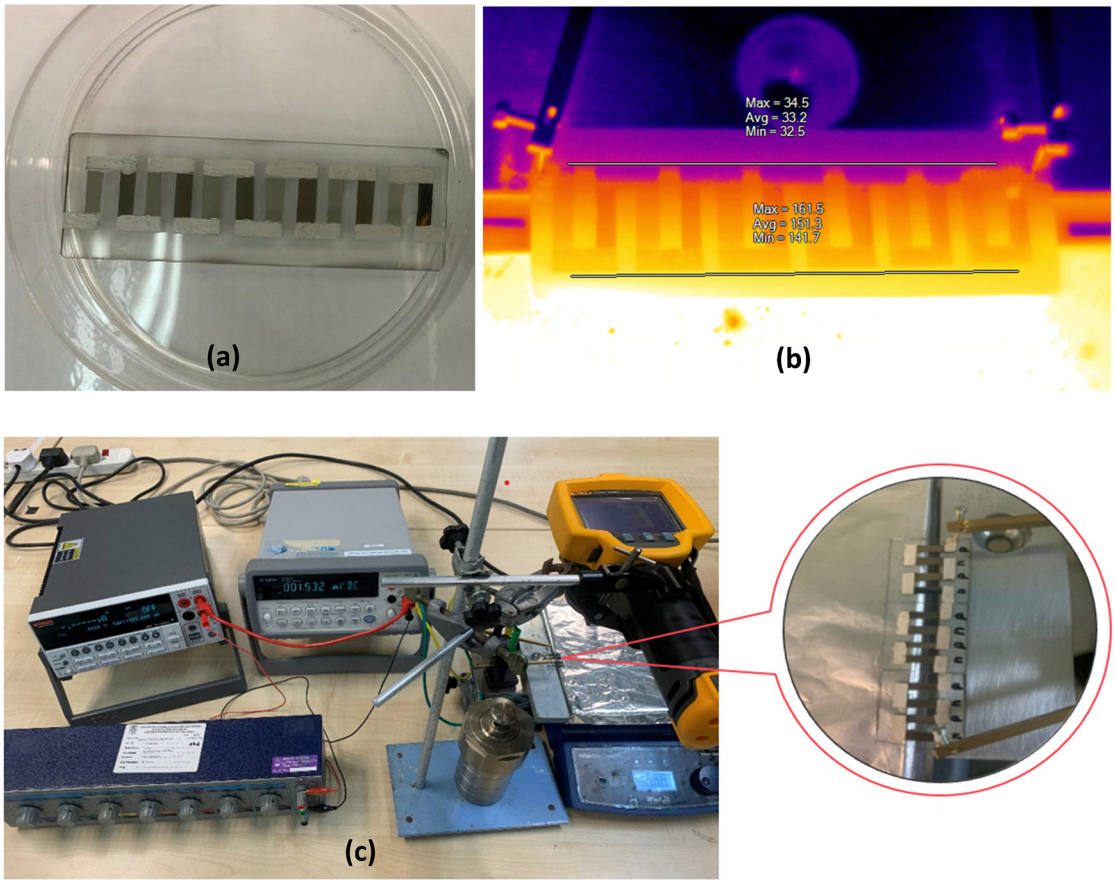

Fig. 2 (a) The fabricated Bi_2Te_3/Sb_2Te_3 thin film TEG. (b) Thermal image of a Bi_2Te_3/Sb_2Te_3 thin film TEG in operation. (c) Picture of the custom IVP measurement setup.

for the films are attributed to the sample layers and not the substrate. As shown in Fig. 3(a), the XRD measurements indicate a good phase purity for Bi_2Te_3 samples, with no measurable trace of secondary phases. This indicates effective control over the stoichiometry and phase during the deposition process. The XRD reflections observed for Bi_2Te_3 can be indexed with the respective rhombohedral Bi_2Te_3 phase (PDF #00-015-0863) in the space group $R\bar{3}m$ (166) with lattice parameters a = 4.3852 Å and c = 30.4830 Å. The observed reflections illustrate preferential growth along the c-axis with a sharp dominant peak growing anisotropically along the (0 1 5) direction, indicating a highly crystalline structure with a few small peaks corresponding to the (0 0 6), (1 0 10) and (1 1 0) directions. The intensity of these peaks systematically increases with RF power, indicating enhanced crystallinity as the RF power increases from 75 W to 135 W. This trend suggests that a higher RF power provides sufficient energy to atoms, promoting surface mobility and the formation of larger, well-ordered grains. This trend can also be seen more clearly in the Sb_2Te_3 spectra.

For Sb_2Te_3 samples (Fig. 3(b)), the peaks aligned well with the respective rhombohedral Sb_2Te_3 phase (PDF #01-071-0393) in the space group $R\bar{3}m$ (166) with lattice parameters a = 4.2640 Å and c = 30.4580 Å. The absence of extraneous peaks in the spectra confirmed that the films are phase-pure Sb_2Te_3 with no detectable secondary phases or impurities. The peaks are relatively small and broad, corresponding to the (0 1 5) direction especially at a low RF power due to the low thickness of the film, as proven by the FESEM cross-section image to be discussed. The intensity of these peaks also increases with RF power from 10 W to 50 W. At lower powers, the peaks are broader and less intense, reflecting poorer crystallinity and smaller crystallite sizes. In contrast, the peaks at 50 W are the sharpest with a notable increment at (1 1 0), highlighting optimal conditions for achieving high-quality crystalline films. Overall, the systematic improvement in peak sharpness and intensity with increasing power highlights the critical role of power optimization in determining the structural properties of the films.

Table 1 presents the crystallite sizes of Bi_2Te_3 and Sb_2Te_3 thin films sputtered at different RF powers. A clear trend emerges where the crystallite size increases from 8.52 nm (sample A1) to 9.59 nm (sample E1) as the sputtering power is increased. This behaviour can be attributed to the higher energy imparted to the sputtered atoms at elevated RF powers, which enhances atom mobility on the substrate surface.[22] As a result, the atoms have more opportunity to diffuse, leading to larger grains during film growth. Although the overall differences in crystallite size are within a narrow range, even slight increases

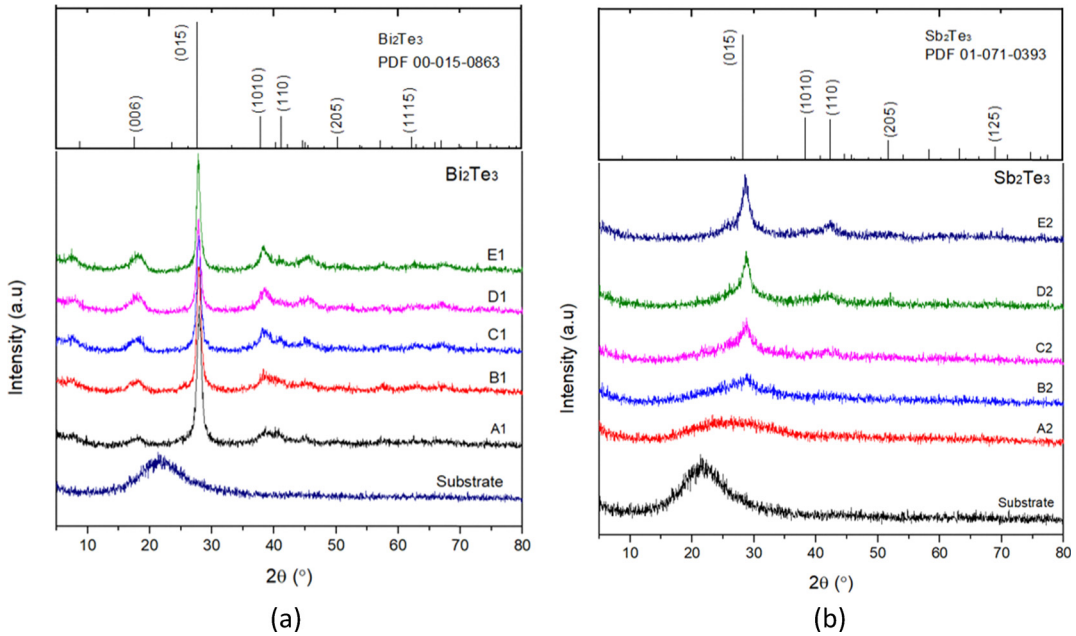

Fig. 3 XRD patterns of (a) Bi_2Te_3 films deposited at 75, 90, 105, 120, and 135 W and (b) Sb_2Te_3 films deposited at 10, 20, 30, 40, and 50 W.

Table 1 Crystallite size and thickness of the Bi_2Te_3 and Sb_2Te_3 films

Material	Sample	RF power, W	Crystallite size, nm	Thickness, μm
Bi_2Te_3	A1	75	8.52	1.429
	B1	90	8.57	1.742
	C1	105	8.88	1.909
	D1	120	9.46	1.945
	E1	135	9.59	2.077
Sb_2Te_3	A2	10	0.91	0.139
	B2	20	1.28	0.365
	C2	30	2.46	0.458
	D2	40	3.08	0.640
	E2	50	3.60	0.938

in grain size can influence the electrical and thermal properties of Bi_2Te_3. Consequently, selecting an appropriate sputtering power becomes critical for optimizing film quality and, by extension, the thermoelectric performance of the deposited layers. A similar trend emerges in the Sb_2Te_3 films: the crystallite size increases from 0.91 nm (sample A2) at 10 W to 3.60 nm (sample E2) at 50 W. Compared to Bi_2Te_3, Sb_2Te_3 films exhibit notably smaller crystallite dimensions. This discrepancy can be attributed to several factors, including the lower overall power range used for Sb_2Te_3 deposition, differences in material composition, and variations in growth kinetics. These results underscore the importance of tailoring sputtering parameters to each specific material system to achieve the desired microstructure and, consequently, optimal thermoelectric performance.

The FESEM micrograph shows that the as-deposited Bi_2Te_3 and Sb_2Te_3 films cover the entirety of the substrate in a continuous and homogenous manner. As can be seen in Fig. 4(a), Bi_2Te_3 films comprise hexagonal grains, confirming the crystal structure of Bi_2Te_3. The grains are densely packed with varying sizes, indicating a polycrystalline nature. The surface of the Sb_2Te_3 film (Fig. 4(b)) exhibits more fine, rounded grains and is consistent in size compared to that of the Bi_2Te_3 film, indicating a nearly amorphous phase resulting in a low and broad peak in XRD. The FESEM surface images presented correspond to Bi_2Te_3 deposited at 75 W for 60 minutes and Sb_2Te_3 deposited at 30 W for 120 minutes. Since the surface morphology of the other films exhibited similar structural characteristics, their images are not included in the main text. Likewise, the FESEM cross-section images used for thickness estimation are omitted, as the measured values are summarized in Table 1. The complete set of FESEM images for all samples is available in the supplementary file for reference. From the cross-sectional views shown in Fig. 4(b) and (e), the interface between the film and the substrate looks distinct, suggesting good adhesion properties. The thickness of the Bi_2Te_3 and Sb_2Te_3 films shows a clear correlation with RF power, where a higher RF power results in increased film thickness. For Bi_2Te_3, the thickness ranges from 1.429 μm at 75 W to 2.077 μm at 135 W, indicating a steady increase with increasing power. Similarly, for Sb_2Te_3, the thickness increases from 0.139 μm at 10 W to 0.938 μm at 50 W. The observed trends are consistent with typical RF sputtering behaviour, where increased power enhances the kinetic energy of the sputtered species, leading to higher deposition rates.[23,24] However, while thicker films may improve mechanical stability, they can also influence electrical and thermal transport properties, which must be carefully optimized for thermoelectric applications.

The EDX spectra of both Bi_2Te_3 and Sb_2Te_3 thin films provide crucial insights into the elemental composition and purity of the deposited materials. In the case of Bi_2Te_3, the spectrum shows prominent peaks corresponding to bismuth (Bi) and tellurium (Te), with their respective weight percentages

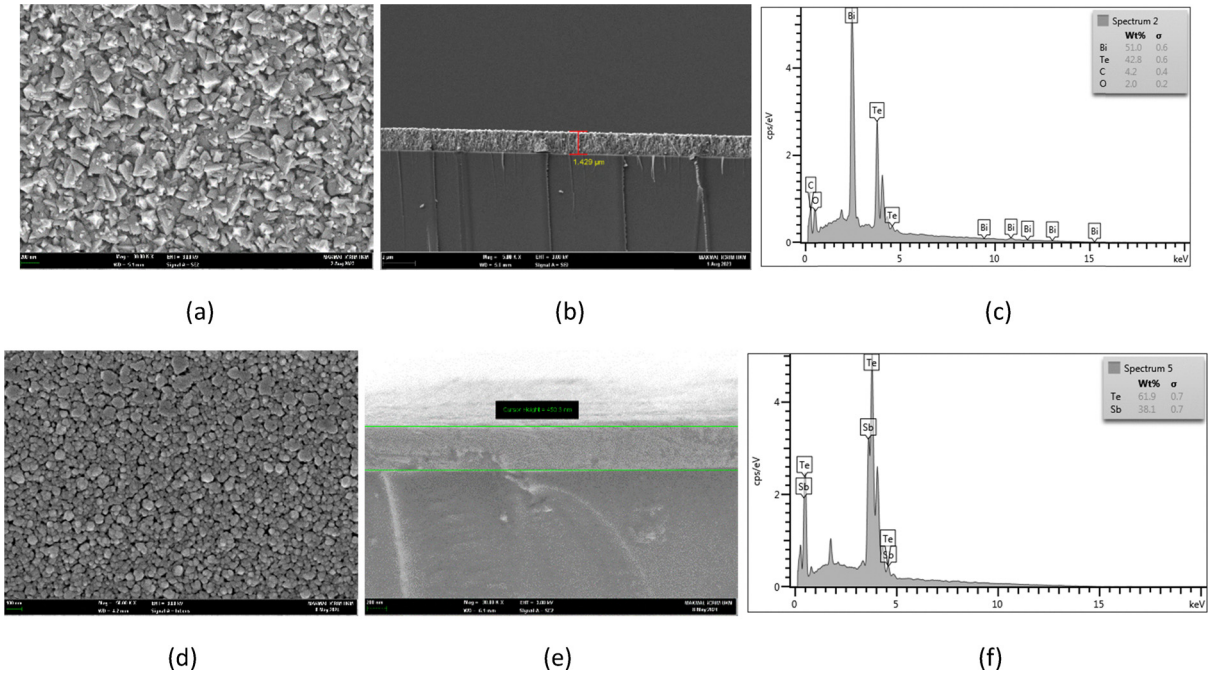

Fig. 4 FESEM surface, cross-section and EDX spectra of the (a)–(c) Bi_2Te_3 and (d)–(f) Sb_2Te_3 films.

of 51.0% and 42.8%. Additionally, small traces of carbon (4.2%) and oxygen (2.0%) are observed, likely due to surface contamination or oxidation. The composition of the films was calculated from the EDX spectra, shown in Fig. 4(c), giving an atomic percent of 41.9% Bi: 58.1% Te. The near-stoichiometric Bi–Te ratio suggests a well-formed Bi_2Te_3 structure, which is desirable for thermoelectric applications. Similarly, the Sb_2Te_3 spectrum exhibits dominant peaks of antimony (Sb) and tellurium (Te), with weight percentages of 38.1% and 61.9%, respectively. The composition of the films was calculated from the EDX spectra, shown in Fig. 4(f), giving an atomic percent of 40.0% Sb:60.0% Te. The estimated values show that the film gave a consistent Sb:Te ratio of 2:3, indicating that stoichiometric Sb_2Te_3 was successfully fabricated. The EDX spectra presented here are representative of the Bi_2Te_3 and Sb_2Te_3 thin films, as the atomic compositions for the other samples exhibit similar elemental distributions. Due to this consistency, the EDX results for the remaining samples are not included in the main text but will be provided in the supplementary file for reference.

3.2. Thermoelectric properties of the Bi_2Te_3 and Sb_2Te_3 thin films

Fig. 5(a) illustrates the variation in σ and carrier concentration of the deposited Bi_2Te_3 thin films. Electrical conductivity, represented by the black plot, increases steadily with RF power, starting at approximately 100 $(\Omega\ cm)^{-1}$ for sample A1 and reaching over 350 $(\Omega\ cm)^{-1}$ for sample E1. This enhancement in σ is attributed to improvements in the structural quality of

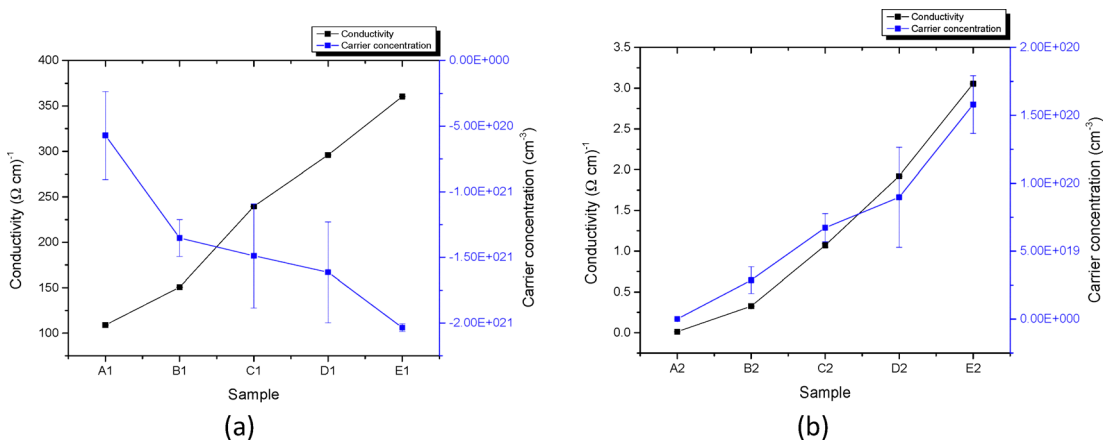

Fig. 5 Conductivity and carrier concentration of (a) n-type Bi_2Te_3 (shown as negative values to indicate electron carriers) and (b) p-type Sb_2Te_3 thin films.

the films, as revealed by the XRD results. At a lower RF power, the XRD spectra display broader and weaker peaks, indicating lower crystallinity and smaller grain sizes. These features increase grain boundary scattering, thereby hindering charge carrier transport.[25] In contrast, at a higher RF power, the diffraction peaks become sharper and more intense, reflecting improved crystallinity and larger grain sizes, which reduce grain boundary scattering and enable better charge transport. Moreover, FESEM analysis shows that film thickness increases with RF power, providing more carriers for charge conduction and further enhancing σ.[26]

The carrier concentration, represented by the blue squares, exhibits an increasingly negative trend with a higher RF power. The carrier concentration measured using Hall effect measurements is derived from the Hall coefficient (R_H). The sign and magnitude of the Hall coefficient provide crucial information about the type and density of charge carriers present in the material.[27] Specifically, a positive Hall coefficient indicates that the majority charge carriers are holes, identifying the material as p-type, whereas a negative Hall coefficient signifies that majority charge carriers are electrons, indicating n-type conductivity. Hence, the negative magnitude in the figure indicates the n-type conductivity of Bi_2Te_3, and the carrier concentration value is actually increasing at a higher RF power. At a lower RF power (75 W, sample A1), the carrier concentration is approximately 5.71×1020 cm^{-3}, and it changes to around 2.03×1021 cm^{-3} at 135 W (sample E1).

The same trends were observed for Sb_2Te_3 thin films (Fig. 5(b)). Both σ and carrier concentration increase consistently with a higher RF power. Specifically, sample A2 shows the lowest σ and carrier concentration, while sample E2 demonstrates the highest values for both parameters. The magnitude of the carrier concentration shows positive values, indicating p-type conductivity for all samples. Overall, the results confirm that increasing RF power enhances the structural and electrical properties of Sb_2Te_3 thin films by improving crystallinity and increasing thickness, leading to higher σ and carrier concentration.

The S plot of Bi_2Te_3 thin films (Fig. 6(a)) deposited at various RF powers demonstrates the dependence of thermoelectric properties on deposition parameters. The negative values of absolute S across all samples confirmed that the films exhibit n-type conductivities, where electrons serve as the dominant charge carriers, consistent with Hall effect measurements. The S value increases with increasing temperature for all samples. This trend indicates a favourable thermoelectric response with temperature, which is associated with grain growth at elevated temperatures,[28] leading to reduced carrier scattering.[29]However, it should be noted that a comprehensive evaluation of thermoelectric performance requires consideration of electrical and thermal conductivities in addition to S.

At near room temperature, sample A1 shows the highest absolute S, approximately -60 μV K^{-1}, indicating superior thermoelectric performance compared to other samples. The higher magnitude of the S suggests a more significant contribution of charge carrier diffusion to the thermoelectric voltage, which is beneficial for energy conversion efficiency. The higher S of sample A1 can be correlated with its relatively lower carrier concentration, as shown in Fig. 5(a). According to the Pisarenko relation, the S is inversely related to carrier concentration, whereby a reduction in carrier density enhances the energy dependence of carrier transport and thus increases the Seebeck value.[30] A lower RF power during deposition resulted in a finer grain structure and a moderate carrier concentration, balancing σ and thermoelectric performance. In contrast, samples deposited at higher RF powers, such as sample E1, show reduced S, due to increased carrier concentrations that lower the thermoelectric voltage.

Fig. 6(b) demonstrates the S plot of Sb_2Te_3 thin films, deposited using RF powers ranging from 10 W (sample A2) to 50 W (sample E2). The positive values of S for all samples confirm the p-type conductivity of the thin films, where holes act as the primary charge carriers. This observation aligns with the intrinsic behaviour of Sb_2Te_3, a well-known p-type thermoelectric material. Sample A2 exhibits an unusually high S near room temperature, exceeding the expected range, due to instrument limits. The conductivity of sample A2 is too low, falling below the resistance limit of the Seebeck instrument. As a result, the measured value lies outside the expected range,

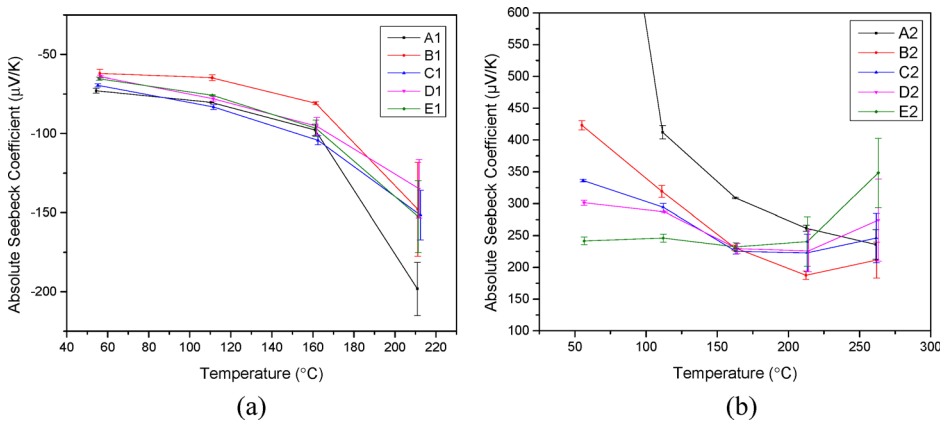

Fig. 6 Seebeck coefficient of (a) Bi_2Te_3 and (b) Sb_2Te_3 thin films.

making the said measurement unreliable. However, as the temperature increases, the S stabilizes and shows improved consistency, suggesting that the carrier transport mechanisms become more favourable at higher temperatures. This trend indicates a strong dependence of thermoelectric performance on the deposition conditions, with a low RF power significantly affecting carrier concentration or scattering. The S of the Sb_2Te_3 thin films exhibits a distinct trend where it decreases with increasing temperature up to a certain point and then starts to increase again at higher temperatures. These results suggest a relatively stable thermoelectric performance for Sb_2Te_3, although the slight decrease indicates some temperature dependence, attributed to the amorphous–crystalline transition. Similar behaviour has also been reported by Fang *et al.*[30] and V. Damodara *et al.*[31,33]

The σ and S of the thin films were determined to calculate the power factor (*PF*) of each film. *PF* becomes a decisive parameter for the selection of thin film materials due to its configuration. A low thermal conductivity is ideal for high efficiency; however, the substrate typically dominates thermal transport in thin film configurations because of the significant difference in thickness.[32] Table 2 shows the calculated power factors of each sample at ambient temperature.

The S and σ values greatly influenced the *PF* of thermoelectric materials, calculated by $PF = S^2\sigma$. However, these two properties exhibit an inverse relationship due to their mutual dependence on carrier concentration, where an increase of one promotes a decrease of the other.[33] The trend in the data reflects the well-known trade-off between these two properties.

For Bi_2Te_3, both σ and S exhibit variations across different samples, influencing the power factor. The trend shows that as conductivity increases (from 108.96 $(\Omega\ cm)^{-1}$ in sample A1 to 360.46 $(\Omega\ cm)^{-1}$ in sample E1), S generally decreases (from 72.84 $\mu V\ K^{-1}$ to 65.33 $\mu V\ K^{-1}$). However, this reduction in S is not steep enough to significantly lower the power factor. As a result, the power factor increases progressively from sample A1 (0.5781 $\mu W\ K^2\ cm^{-1}$) to sample E1 (1.5384 $\mu W\ K^2\ cm^{-1}$). This suggests that increasing σ plays a dominant role in improving the thermoelectric performance of Bi_2Te_3.

For Sb_2Te_3, the opposite trend is observed compared to Bi_2Te_3. The S is significantly higher in samples with lower σ, particularly in sample A2, but σ is very low (0.01067$(\Omega\ cm)^{-1}$), leading to a very small power factor (0.0163 $\mu W\ K^2\ cm^{-1}$). As σ increases from sample A2 to sample E2, S decreases sharply, from 1236.84 $\mu V\ K^{-1}$ to 241.56 $\mu V\ K^{-1}$. While σ increases significantly (from 0.01067 to 3.055 $(\Omega\ cm)^{-1}$), the strong reduction in S limits the power factor improvement. Consequently, the power factor increases but at a much lower rate than in Bi_2Te_3, reaching a maximum of 0.1783 $\mu W\ K^2\ cm^{-1}$ in sample E2. These results highlight that optimizing thermoelectric performance depends on finding a balance between σ and S.

The results obtained above guide the selection of the deposition parameters for device fabrication. While certain parameters yield higher *PF* values, other factors such as stability, reproducibility, and temperature-dependent behavior must also be considered. Achieving a balance between these aspects ensures that the fabricated device performs efficiently across a range of operating conditions. For the fabrication of the TEG, sample A (Bi_2Te_3) was selected due to its higher S near room temperature, which is critical for applications operating across ambient-to-moderate temperature gradients. This characteristic ensures sustained thermoelectric performance and contributes to a higher thermoelectric figure of merit (*ZT*). For the Sb_2Te_3 layer, sample C was chosen owing to its stable and consistent thermoelectric behaviour across the measured temperature range, offering a reliable balance between efficiency and operational stability. Although some samples exhibited higher *PF*, the selection was primarily guided by S trends, given that Hall measurements were limited to room temperature. The chosen samples demonstrated an optimal combination of initial S values, thermal stability, and structural integrity, ensuring enhanced efficiency, reliability, and practical applicability of the optimized TEG device.

3.3. Performance analysis of the Bi_2T_3/Sb_2Te_3 thin film TEG

In this section, the fabrication of a TEG with 6 pairs of n-type Bi_2Te_3 and p-type Sb_2Te_3 with optimal deposition parameters studied above is described, and its performance was analysed. The measurement of ΔT *versus* V_{oc} was done in the temperature range of 100–200 °C, with a 10 °C increment, although the measured ΔTs did not fully match the set temperature of T_h and T_c due to the poor heat sink setup and heat dispersion on the hotplate. Fig. 7(a) demonstrates a linear relationship

Table 2 Conductivity, absolute Seebeck coefficient and power factor of each sample at ambient temperature

Material	Sample	Conductivity, σ $(\Omega\ cm)^{-1}$	Absolute Seebeck coefficient, S $(\mu V\ K^{-1})$	Power factor, PF $(\mu W\ K^{-2}\ cm^{-1})$
Bi_2Te_3	A1	108.96	72.84	0.5781
	B1	150.6	62.02	0.5793
	C1	239.46	69.43	1.1543
	D1	295.92	64.03	1.2132
	E1	360.46	65.33	1.5384
Sb_2Te_3	A2	0.01067	(OOR)	
	B2	0.32594	423.43	0.1584
	C2	1.0696	336.11	0.1208
	D2	1.9206	301.44	0.1745
	E2	3.055	241.56	0.1783

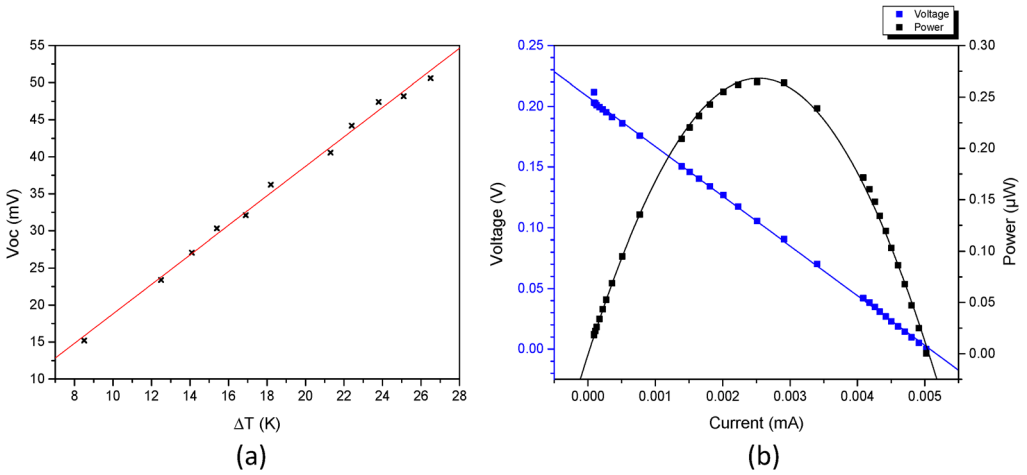

Fig. 7 (a) V_{oc} *vs.* ΔT and (b) IVP plot of the optimized Bi_2Te_3/Sb_2Te_3 thin film TEG.

between V_{oc} and the applied ΔT, indicating the typical and ideal response of a TEG.[34] The steepness of the slope reflects a high S, suggesting that the TEG material efficiently converts the thermal gradient into an electrical voltage. Under these conditions, the TEG composed of 6 n–p leg pairs achieved a noteworthy maximum V_{oc} of 50.59 mV at a ΔT of 26.5 K. Fig. 7(b) shows the current–voltage (*IV*) and the current–power (*IP*) curve of the optimized Bi_2Te_3/Sb_2Te_3 thin film TEG. The Bi_2Te_3/Sb_2Te_3 thin film TEG achieved a peak power output of 0.26 μW at 0.0025 mA under a ΔT of $\sim$ 120 °C. When normalized to the active planar area and number of TE legs, the maximum power density was calculated to be 0.05 μW cm^{-2}. While this output is modest compared to vertically structured or heavily engineered TEGs, it aligns well with the performance reported for planar thin films employing comparable material systems and fabrication methods.[35–38]

3.4. Annealing effect on the performance of the Bi_2T_3/Sb_2Te_3 thin film TEG

Fig. 8(a) shows the IV characteristics of the optimized Bi_2Te_3/Sb_2Te_3 thin-film thermoelectric generator (TEG) annealed at 100 °C and 200 °C. The sample annealed at 200 °C (A200) shows a lower slope compared to the other conditions, indicating a lower internal resistance. This suggests that annealing at 200 °C improves σ, due to enhanced crystallinity and reduced grain boundary scattering.[39–41] On the other hand, the sample annealed at 100 °C (A100) exhibits a slightly higher resistance than the optimized sample.[44]

Fig. 8(b) exhibits the IP plot, illustrating the power output as a function of current for the optimized Bi_2Te_3/Sb_2Te_3 thin-film TEG annealed at different temperatures. The curves show distinct power–current characteristics, indicating the influence of annealing temperature on the TEG's performance. Among the three samples, the TEG annealed at 200 °C (A200) exhibits the highest power output, peaking at 0.84 μW at around 0.012 mA. This indicates that higher annealing temperatures enhance the σ and overall thermoelectric efficiency of the device. This improvement is due to enhanced crystallinity, reduced grain boundary scattering, and optimized carrier concentration, which collectively contribute to better charge transport properties, confirming that the reduced internal resistance contributes to improved electrical performance.

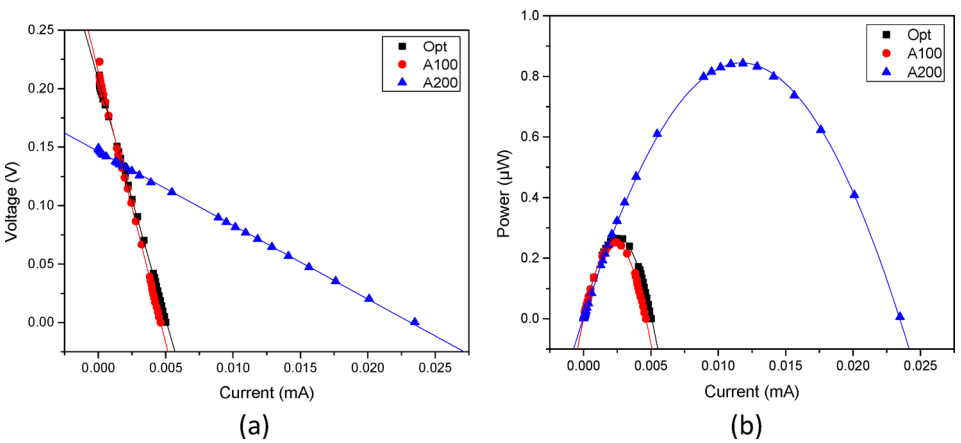

Fig. 8 (a) IV and (b) IP plots of the optimized Bi_2Te_3/Sb_2Te_3 thin film TEG, annealed at 100 and 200 °C.

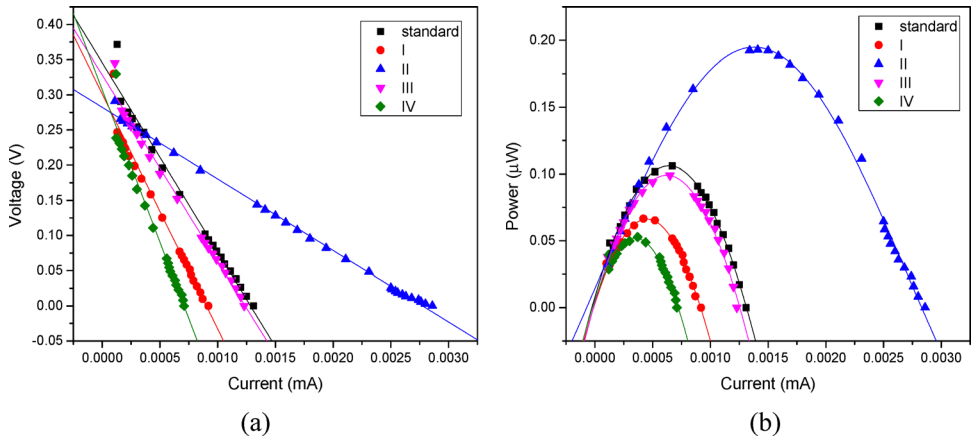

Fig. 9 (a) IV and (b) IP plots of the Sb_2Te_3-only thin film TEG with different dimensions.

In contrast, the TEG annealed at 100 °C (A100) demonstrates a slight reduction in power output compared to the optimized sample, 0.25 μW at around 0.003 mA, aligning with the IV results where increased resistance may have caused power dissipation. This behavior can be correlated with the S trends shown in Fig. 6, where Bi_2Te_3 (sample A1) shows only a modest increase in Seebeck value when the temperature increases to 100 °C, while Sb_2Te_3 (sample C2) experiences a more pronounced reduction. Since the overall device voltage and power are determined by the combined contributions of both p-type and n-type legs, the significant degradation in the Sb_2Te_3 S offsets the minor improvement in Bi_2Te_3, resulting in a net decrease in thermoelectric performance at 100 °C. Thus, annealing at 200 °C appears to optimize the material properties, leading to enhanced thermoelectric efficiency.

3.5. Dimensional optimization of the TEG

Fig. 9(a) shows the voltage–current characteristics of Sb_2Te_3-only thin film TEGs with different dimensions, including a standard design. All measurements were done at a ΔT of approximately 120 °C. The slope of each curve represents the internal resistance of the TEG, which is influenced by the length and width of the legs. Longer legs, such as the 25 mm and 35 mm designs, exhibit a higher internal resistance compared to the standard 15 mm legs. This is because resistance increases with length, as expressed by the formula,

$$R = \rho\frac{L}{A},$$

where ρ is the resistivity and A is the cross-sectional area. While lengthening the legs can enhance thermal resistance and broaden the temperature gradient (boosting voltage), it simultaneously increases electrical resistance, resulting in diminished output current and steeper IV slopes.[42,43]On the other hand, the width of the legs also plays a crucial role. The narrower 1.5 mm legs exhibit higher resistance due to a smaller cross-sectional area, which restricts current flow and results in steeper IV slopes. In contrast, the wider 4.5 mm legs have lower resistance, allowing more current to flow and producing a flatter IV slope. This trend follows the inverse relationship of resistance with cross-sectional area, where a larger area reduces resistive losses.[44]

Fig. 9(b) shows the IP curve of Sb_2Te_3-only thin film TEGs with different dimensions. The wider leg (4.5 mm) produces the highest power output, peaking at 0.19 μW, due to its lower internal resistance, which allows for a higher current flow. On the other hand, narrower legs (1.5 mm) exhibit a significantly lower power output compared to the standard dimension (0.11 μW), peaking at 0.07 μW due to their higher resistance, which restricts current flow and reduces the overall efficiency of the device. For longer legs, the maximum power is reduced, 0.10 μW for 25 mm and 0.05 μW for 35 mm compared to the standard dimensions, as their increased resistance limits current flow despite maintaining a good temperature gradient. From the IVP plot, it is evident that wider legs provide better σ, while longer or narrower legs increase resistance, limiting current output. The results from the dimensional optimization provided valuable and clear insights into the impact of dimension control on the performance of the TEGs, providing a crucial foundation for future research.

4. Conclusion

The thermoelectric properties and performance optimization of Bi_2Te_3 and Sb_2Te_3 thin films for TEG applications have been successfully studied. The results demonstrated that the best strategy for enhancing TEG performance involves careful control of deposition parameters, post-deposition annealing, and dimensional optimization. For Bi_2Te_3 thin films, the optimal RF sputtering conditions were identified as 75 W for 60 minutes, yielding the highest σ and S. For Sb_2Te_3 thin films, the best results were achieved with an RF power of 30 W for 120 minutes, balancing carrier concentration and σ. Post-deposition annealing at 200 °C further improved thermoelectric performance by enhancing crystallinity and reducing grain boundary scattering, leading to increased power output and overall efficiency. Dimensional optimization revealed that wider and shorter thermoelectric legs minimized internal resistance while maintaining effective thermal gradients, maximizing power

generation. These findings highlight the importance of a holistic approach that combines material optimization, thermal treatment, and geometric design to achieve high-efficiency TEGs. The continuation of this study should prioritize several key areas to enhance their performance and broaden their applications, such as accurately measuring the thermal conductivity of the films to understand the overall thermoelectric efficiency, systematically investigating the effect of film thickness on thermoelectric performance and exploring doping or alloying Bi_2Te_3 and Sb_2Te_3 with other elements, such as In or Mn, that could further optimize the S, σ, and thermal stability.

Conflicts of interest

There are no conflicts to declare.

Data availability

The data supporting this article have been included as part of the supplementary information (SI). Supplementary information is available. See DOI: https://doi.org/10.1039/d5ma00823a.

Acknowledgements

The authors would like to acknowledge the financial support from the Universiti Kebangsaan Malaysia research grant, under Project Number: GGPM-2022-069 to carry out this research.

References

1 F. D. Rosi, Thermoelectricity and Thermoelectric Power Generation, *Solid-State Electron.*, 1968, **11**(9), 833–868, DOI: 10.1016/0038-1101(68)90104-4.
2 M. Al-Widyan, M. Al-Nimr and Q. Al-Oweiti, A hybrid TEG/Thermal radiator system for space heating and electric power generation, *J. Build. Eng.*, 2021, **41**, 102364, DOI: 10.1016/j.jobe.2021.102364.
3 J. He, K. Li, L. Jia, Y. Zhu, H. Zhang and J. Linghu, Advances in the applications of thermoelectric generators, *Appl. Therm. Eng.*, 2024, 236, DOI: 10.1016/j.applthermaleng.2023.121813.
4 G. Pennelli, E. Dimaggio and M. Macucci, Electrical and thermal optimization of energy-conversion systems based on thermoelectric generators, *Energy*, 2022, **240**, 122494, DOI: 10.1016/j.energy.2021.122494.
5 A. O. Ochieng, T. F. Megahed, S. Ookawara and H. Hassan, Comprehensive review in waste heat recovery in different thermal energy-consuming processes using thermoelectric generators for electrical power generation, *Process Saf. Environ. Prot.*, 2022, **162**, 134–154, DOI: 10.1016/j.psep.2022.03.070.
6 M. A. Qasim, V. I. Velkin, S. E. Shcheklein, S. A. Salih, B. A. Aljashaami and A. A. Sammour, Conversion of Heat Generated During Normal PV Panel Operation into Useful Energy via a Hybrid PV-TEG Connection, *Int. J. Renewable Energy Res.*, 2022, **12**(4), 1779–1786, DOI: 10.20508/ijrer.v12i4.13471.g8603.
7 J. He, K. Li, L. Jia, Y. Zhu, H. Zhang and J. Linghu, Advances in the applications of thermoelectric generators, *Appl. Therm. Eng.*, 2024, 236, DOI: 10.1016/j.applthermaleng.2023.121813.
8 E. Isotta, J. Andrade-Arvizu and U. Syafiq, *et al.*, Towards Low Cost and Sustainable Thin Film Thermoelectric Devices Based on Quaternary Chalcogenides, *Adv. Funct. Mater.*, 2022, **32**(32), 2202157, DOI: 10.1002/adfm.202202157.
9 J. Wei, L. Yang and Z. Ma, *et al.*, Review of current high-ZT thermoelectric materials. *J. Mater. Sci.*, 2020;55(27):12642–12704. , DOI: 10.1007/s10853-020-04949-0.
10 T. Cao, X. L. Shi and M. Li, *et al.*, Advances in bismuth-telluride-based thermoelectric devices: Progress and challenges, *eScience*, 2023, **3**(3), 100122, DOI: 10.1016/j.esci.2023.100122.
11 A. Kim, P. Kumar, P. K. Annamalai and R. Patel, Recent Advances in the Nanomaterials, Design, Fabrication Approaches of Thermoelectric Nanogenerators for Various Applications, *Adv. Mater. Interfaces*, 2022, **9**(35), 2201659, DOI: 10.1002/admi.202201659.
12 Y. Jia, Q. Jiang and H. Sun, *et al.*, Wearable Thermoelectric Materials and Devices for Self-Powered Electronic Systems, *Adv. Mater.*, 2021, **33**(42), 2102990, DOI: 10.1002/adma.202102990.
13 Z. H. Zheng, X. L. Shi and D. W. Ao, *et al.*, Harvesting waste heat with flexible Bi2Te3 thermoelectric thin film, *Nat. Sustainable*, 2022, **6**(2), 180–191, DOI: 10.1038/s41893-022-01003-6.
14 Z. Wu, X. Chen and E. Mu, *et al.*, Lattice Strain Enhances Thermoelectric Properties in Sb 2 Te 3/Te Heterostructure, *Adv. Electron. Mater.*, 2020, **6**(1), 1900735, DOI: 10.1002/aelm.201900735.
15 S. A. Haidar, Y. Gao and Y. He, *et al.*, Deposition and Fabrication of Sputtered Bismuth Telluride and Antimony Telluride for Microscale Thermoelectric Energy Harvesters, *Thin Solid Films*, 2021, **717**, 138444, DOI: 10.1016/j.tsf.2020.138444.
16 A. Khalil, A. Elhassnaoui, S. Yadir, O. Abdellatif, Y. Errami and S. Sahnoun, Performance comparison of TEGs for diverse variable leg geometry with the same leg volume, *Energy*, 2021, **224**, 119967, DOI: 10.1016/j.energy.2021.119967.
17 N. Kuang, Z. Zuo, W. Wang, R. Liu and Z. Zhao, Optimized thermoelectric properties and geometry parameters of annular thin-film thermoelectric generators using n-type Bi2Te2.7Se0.3 and p-type Bi0.5Sb1.5Te3 thin films for energy harvesting, *Sens. Actuators A*, 2021, **332**, 113030, DOI: 10.1016/j.sna.2021.113030.
18 D. W. Newbrook, R. Huang and S. P. Richards, *et al.*, Mathematical model and optimization of a thin-film thermoelectric generator, *JPhys Energy*, 2020, **2**(1), 014001, DOI: 10.1088/2515-7655/ab4242.
19 M. Ohring, *Materials Science of Thin Films*, Elsevier, 2002. , DOI: 10.1016/B978-0-12-524975-1.X5000-9.

20 N. A. Musri, Y. Putthisigamany, P. Chelvanathan, N. Ahmad Ludin, N. Md Yatim and U. Syafiq, Fabrication of Bi_2Te_3 and Sb_2Te_3 Thermoelectric Thin Films using Radio Frequency Magnetron Sputtering Technique, *J. Visualized Exp.*, 2024, 2024(207), DOI: 10.3791/66248.
21 N. Ahmad Musri, Y. Putthisigamany, P. Chelvanathan, N. Ahmad Ludin, N. Md Yatim and U. Syafiq, Fabrication and Performance Analysis of Bi2Te3 and Sb2Te3 Thin Film Thermoelectric Generator for Waste Heat Recovery, *J. Climate Change*, 2025, **11**(2), 13, DOI: 10.70917/jcc-2025-012.
22 J. M. Lugo, E. Rosendo and R. Romano-Trujillo, *et al.*, Effects of the applied power on the properties of RF-sputtered CdTe films, *Mater. Res. Express*, 2019, **6**(7), DOI: 10.1088/2053-1591/ab17c0.
23 A. Baptista, F. Silva, J. Porteiro, J. Míguez and G. Pinto, Sputtering physical vapour deposition (PVD) coatings: A critical review on process improvement and market trend demands, *Coatings*, 2018, **8**(11), 402, DOI: 10.3390/COATINGS8110402.
24 Y. H. Wang, K. H. Rahman, C. C. Wu and K. C. Chen, A review on the pathways of the improved structural characteristics and photocatalytic performance of titanium dioxide (TiO2) thin films fabricated by the magnetron-sputtering technique, *Catalysts*, 2020, **10**(6), 598, DOI: 10.3390/catal10060598.
25 C. Hu, K. Xia, C. Fu, X. Zhao and T. Zhu, Carrier grain boundary scattering in thermoelectric materials, *Energy Environ. Sci.*, 2022, **15**(4), 1406–1422, DOI: 10.1039/D1EE03802H.
26 Y. Yin and A. Tiwari, Understanding the effect of thickness on the thermoelectric properties of Ca3Co4O9 thin films, *Sci. Rep.*, 2021, **11**(1), 6324, DOI: 10.1038/s41598-021-85287-2.
27 Y. Xu, Thermoelectric effects and topological insulators, *Chin. Phys. B*, 2016, **25**(11), 117309, DOI: 10.1088/1674-1056/25/11/117309.
28 Y. Zhao, L. Li and Z. Lu, *et al.*, The effect of annealing temperature on the recrystallization and mechanical properties of severe plastic deformed commercial pure aluminium during ultra-fast annealing, *Mater. Res. Express*, 2021, **8**(4), 046515, DOI: 10.1088/2053-1591/abf3e3.
29 J. Zang, Y. Ma and Y. Zhao, *et al.*, Effect of post-annealing treatment on the thermoelectric properties of Ag2Se flexible thin film prepared by magnetron sputtering method, *Results Phys.*, 2023, **45**, 106222, DOI: 10.1016/j.rinp.2023.106222.
30 B. Fang, Z. Zeng, X. Yan and Z. Hu, Effects of annealing on thermoelectric properties of Sb_2Te_3 thin films prepared by radio frequency magnetron sputtering, *J. Mater. Sci.: Mater. Electron.*, 2013, **24**(4), 1105–1111, DOI: 10.1007/s10854-012-0888-1.
31 V. Damodara Das, N. Soundararajan and M. Pattabi, Electrical Conductivity and Thermoelectric Power of Amorphous Sb_2Te_3 Thin Films and Amorphous-Crystalline Transition, *J. Mater. Sci.*, 1987, **22**(10), 3522–3528, DOI: 10.1007/BF01161452.
32 E. Isotta, J. Andrade-Arvizu and U. Syafiq, *et al.*, Towards Low Cost and Sustainable Thin Film Thermoelectric Devices Based on Quaternary Chalcogenides, *Adv. Funct. Mater.*, 2022, **32**(32), 2202157, DOI: 10.1002/adfm.202202157.
33 J. D. Musah, A. M. Ilyas and A. Novitskii, *et al.*, Effective decoupling of seebeck coefficient and the electrical conductivity through isovalent substitution of erbium in bismuth selenide thermoelectric material, *J. Alloys Compd.*, 2021, **857**, 157559, DOI: 10.1016/j.jallcom.2020.157559.
34 K. Li, G. Garrison and M. Moore, *et al.*, An expandable thermoelectric power generator and the experimental studies on power output, *Int. J. Heat Mass Transfer*, 2020, **160**, 120205, DOI: 10.1016/j.ijheatmasstransfer.2020.120205.
35 A. Kobayashi, R. Konagaya, S. Tanaka and M. Takashiri, Optimized structure of tubular thermoelectric generators using n-type Bi2Te3 and p-type Sb2Te3 thin films on flexible substrate for energy harvesting, *Sens. Actuators, A*, 2020, **313**, 112199, DOI: 10.1016/j.sna.2020.112199.
36 K. Takayama and M. Takashiri, Multi-layered-stack thermoelectric generators using p-type Sb2Te3 and n-type Bi2Te3 thin films by radio-frequency magnetron sputtering, *Vacuum*, 2017, **144**, 164–171, DOI: 10.1016/j.vacuum.2017.07.030.
37 S. A. Haidar, Y. Gao and Y. He, *et al.*, Deposition and Fabrication of Sputtered Bismuth Telluride and Antimony Telluride for Microscale Thermoelectric Energy Harvesters, *Thin Solid Films*, 2021, **717**, 138444, DOI: 10.1016/j.tsf.2020.138444.
38 D. Kong, W. Zhu, Z. Guo and Y. Deng, High-performance flexible Bi2Te3 films based wearable thermoelectric generator for energy harvesting, *Energy*, 2019, **175**, 292–299, DOI: 10.1016/j.energy.2019.03.060.
39 S. Kianwimol, R. Sakdanuphab, N. Chanlek, A. Harnwunggmoung and A. Sakulkalavek, Effect of annealing temperature on thermoelectric properties of bismuth telluride thick film deposited by DC magnetron sputtering, *Surf. Coat. Technol.*, 2020, **393**, 125808, DOI: 10.1016/j.surfcoat.2020.125808.
40 Z. Zheng, D. Yang and P. C. Zhang, *et al.*, Enhancement of the thermoelectric properties of Bi2Te3 nanocrystal thin films by rapid annealing, *Mater. Lett.*, 2020, **275**, 128143, DOI: 10.1016/j.matlet.2020.128143.
41 M. Naumochkin, G. H. Park, K. Nielsch and H. Reith, Study of the Annealing Effects of Sputtered Bi2Te3 Thin Films with Full Thermoelectric Figure of Merit Characterization, *Phys. Status Solidi RRL*, 2022, **16**(4), 2100533, DOI: 10.1002/pssr.202100533.
42 B. Şişik and S. LeBlanc, The Influence of Leg Shape on Thermoelectric Performance Under Constant Temperature and Heat Flux Boundary Conditions, *Front. Mater.*, 2020, **7**, DOI: 10.3389/fmats.2020.595955.
43 G. G. Dalkiranis, J. H. C. Bocchi, O. N. Oliveira and G. C. Faria, Geometry Optimization for Miniaturized Thermoelectric Generators, *ACS Omega*, 2023, **8**(10), 9364–9370, DOI: 10.1021/acsomega.2c07916.
44 Y. Luo and C. N. Kim, Effects of the cross-sectional area ratios and contact resistance on the performance of a cascaded thermoelectric generator, *Int. J. Energy Res.*, 2019, **43**(6), 2172–2187, DOI: 10.1002/er.4426.